A Compact Visible/Near Infrared Hyperspectral Imager

James E. Murguia, Toby D. Reeves*, Jonathan M. Mooney*, William S. Ewing*, Freeman D. Shepherd, Andrzej Brodzik

Solid State Scientific Corporation
27-2 Wright Road, Hollis NH
jim@solidstatescientific.com

*AFRL/SNHI
Hanscom AFB, Bedford MA
jon@max.rl.plh.af.mil

ABSTRACT

This paper reports on the design, performance and signal processing of a visible/near infrared (VIS-NIR) chromotomographic hyperspectral imaging sensor. The sensor consists of a telescope, a direct vision prism, and a framing video camera. The direct vision prism is a two-prism set, arranged such that one wavelength passes undeviated, while the other wavelengths are dispersed along a line. The prism is mounted on a bearing so that it can be rotated on the optical axis of the telescope. As the prism is rotated, the projected image is multiplexed on elements of the focal plane array. Computational methods are used to reconstruct the scene at each wavelength; an approach similar to the limited-angle tomography techniques used in medicine. The sensor covers the visible through near infrared spectrum of silicon photodiodes. The sensor weighs less than 6 pounds has under 300 in^3 volume and requires 20 watts. It produces image cubes, with 64 spectral bands, at rates up to 10 Hz. By operating in relatively fast framing mode, the sensor allows characterization of transient events. We will describe the sensor configuration and method of operation. We also present examples of sensor spectral image data.

Keywords: Hyperspectral imager, visible to near infrared, chromotomographic processing

1.0 INTRODUCTION

Hyperspectral image sensing detects both the spatial and spectral content of radiation from an observed scene. This is an emerging technology, having significant promise for a broad range of applications, including Earth resource management, reconnaissance, medical diagnostics and industrial process control. Most hyperspectral imagers have been developed for Earth resource mapping and for air and space surveillance. In general, these devices are designed to observe static and slowing changing events, such as crop development, and therefore they have no capability to measure rapid events. However, there is significant untapped potential in the application of hyperspectral imaging to the measurement of transient events and evolving scenarios. Applications range from measurement of lightning activity and detection of the initiation of fires in forest management, to the assessment of the location, intensity and effects of battle conflict. Time resolved hyperspectral imaging may also be applied to detection and tracking of unresolved moving objects.

Effective surveillance of transient events and moving objects adds the requirement fohyperspectral imaging sensors to provide continuous time resolved data, over the entire area of interest. To meet this requirement the sensor optical throughput must be high, to support rapid image update. The sensor must also provide efficient mapping of the region of observation, to assure that transient signals are not missed. We consider whether the three classes of hyperspectral imaging sensor, scanned-slit, optical filter and tomographic, meet the additional requirements for transient event measurement. The relative collection efficiency of these three basic spectral measurement techniques is compared schematically in Figure 1.

Scanned-slit hyperspectral imaging systems are well established. Often, the scanning mechanism is provided by platform motion, making this class of sensor particularly suitable for satellite and aircraft based measurement. These systems operate by dispersing the light from a slit over a two-dimensional focal-plane-array. The image on the focal plane is x-spatial, in the

In *Infrared Detectors and Focal Plane Arrays VI*, Eustace L. Dereniak, Robert E. Sampson, Editors,
Proceedings of SPIE Vol. 4028 (2000) • 0277-786X/00/$15.00

direction of the slit and λ-spectral, normal to the slit. The sensor is scanned normal to the slit, one pixel per measurements interval, to record the y-spatial dimension of the scene. To obtain high spectral resolution, the slit is made narrow. However, a narrow slit limits the amount of light passed by the optical system (the AΩ product), reducing the signal to noise ratio (SNR) of the image. The SNR can be recovered by increasing the exposure interval. These systems have two significant limitations in measuring transient events, partial area coverage and a relatively long exposure interval. Nevertheless, scanned slit instruments provide the baseline against which all other instruments are compared.

Another common method of obtaining hyperspectral images is to observe a scene through a series of spectral filters or through a resonant cavity device, which is swept in wavelength. The optical throughput of this class of sensor is limited by the instantaneous optical bandwidth of the particular filter mechanism. Filtered sensors have good area coverage, but their capability to measure transient events is degraded by lack of synchronization between the spectrum of the event and the instantaneous spectral band-pass of the sensor.

A tomographic sensor can have simultaneous wide area coverage and wide spectral bandwidth. This class of sensor can provide continuous hyperspectral data over a wide image area. In principle, tomographic sensors should be capable of effective hyperspectral imaging surveillance of transients and moving objects. However, the operation of tomographic sensors and the nature of tomographic signals are quite complex, resulting in the need for substantially greater signal and image processing. The potential for time resolved tomographic hyperspectral imaging is determined, or limited, by the processing time to update a spectral data cube. The processing time will be dependent upon the sensor architecture, the 3-dimensional resolution requirement and the availability of fast computer systems and effective algorithms. Mooney et al, have demonstrated a sensor, the CTHIS (Chromotomographic Hyperspectral Imaging Sensor), that has sufficient throughput to measure the time evolved spectra of explosions.[1]

CTHIS is a staring-mode, framing camera system, which encodes both spatial and spectral information on every frame of data. The use of a tomographic measurement technique eliminates the need for a slit, optical filter, or resonant cavity and substantially increases optical throughput. It also eliminates the possibility that an event will occur when the sensor is viewing the wrong portion of the scene. The CTHIS optical throughput, or AΩ product, is determined by the camera field stop. This sensor is appropriate for measuring spectra of scenarios with rapidly evolving events. It also provides the capability to capture point-like transient events over a large field of view. The framing operation of CTHIS samples the spatial and spectral content of the observed scene, over each video frame. This has the effect of expanding the information from the 3-dimensional data cube of hyperspectral imaging, by the adding time as a fourth dimension.

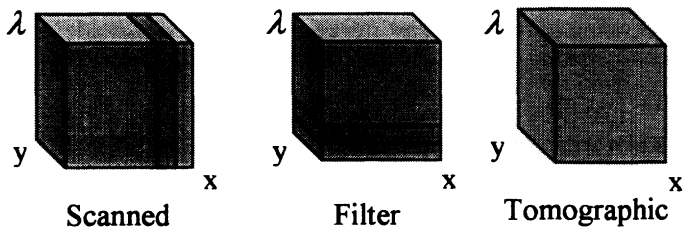

Figure 1: Comparison of hypercube acquisition by scanned slit, filter wheel or interferometer, and tomographic

CTHIS is a Medium Wavelength InfraRed (MWIR) sensor developed by workers at the Air Force Research Laboratory (AFRL) Sensors Directorate, Hanscom AFB, Massachusetts. The choice of MWIR was based on several military applications including detection of aircraft and missile plumes, as well as, long-range thermal imaging. It was also based on AFRL's extensive experience with developing MWIR staring-mode imaging sensors. The AFRL CTHIS is a bread-board instrument, which has been successfully demonstrated in numerous laboratory and ground-based field data collections.[2] Development of the MWIR CTHIS sensor started in 1995. It has evolved through several configurations, as tomographic imaging techniques were developed. The current sensor is a laboratory demonstration instrument with 64 spectral bands, a 1-second data cube acquisition time, liquid nitrogen cooling, and dimensions 32"x9"x6". The camera head is based on a 256x256 InSb array operating at F/4 and 60 frames/second, in the 3-5μm band. No attempt has been made to miniaturize the MWIR sensor.

Solid State Scientific Corporation (SSSC) has adapted the CTHIS architecture to the visible-near infrared spectrum of silicon pn-junction photo-diodes.[3] In fact, the CTHIS architecture should be applicable to any spectral band; given the availability of appropriate materials for the detector array, telescope, and direct-vision prism set. SSSC and AFRL are currently developing a CTHIS sensor for the LWIR that uses an un-cooled micro-bolometer for the imaging array. This uncooled LWIR hyperspectral imager is practical because of the high AΩ product of CTHIS. The SSSC VIS-NIR CTHIS is described below.

2. DESCRIPTION OF THE INSTRUMENT

Figure 2 is a schematic representation of a chromotomographic hyperspectral imaging sensor, consisting of a telescope, a direct vision prism, and a camera. A direct vision prism consists of two prisms that are arranged such that one wavelength passes undeviated, while the other wavelengths are dispersed along a line, or dispersion axis. An image projected onto the focal plane will be dispersed along this axis. The direct vision prism is mounted on a bearing so that it can be rotated on the optical axis of the telescope. During the measurement of successive video frames, the dispersion axis is rotated, causing the image of spectral features to trace out circles with wavelength dependent radii. This has the effect of multiplexing the color information of the image over the array, which, otherwise, is operating as a broad band polychromatic sensor. Examples of the VIS-NIR CTHIS dispersed input imagery, taken during one revolution of the prism set, are given in Figure 2. Tomographic computational methods that are similar to the limited-angle tomography techniques used in medicine are used to reconstruct the scene. A reconstructed broad band image of the observed scene is also given in Figure 2.

The sensor tomographic technique can be summarized as follows. During a video frame, all photons from the observed scene, which pass through the field stop, are detected by the focal plane array. This includes all photons within the spectral response range of the detector. During successive frames, the rotating prism multiplexes spectral features over the focal plane array. Video frames are collected over a full prism rotation. This super-integration requires a de-multiplexing operation to extract the spectral imagery from the measured data. As an added benefit, the mathematical chromotomographic reconstruction simultaneously returns the data cube and the principal components of the spectral image. Note that this allows us to determine:

- the spectrum at each pixel
- the mixture of spectral principal components at each pixel, or across the scene
- spectral slices of the image
- the presence of objects having particular spectra

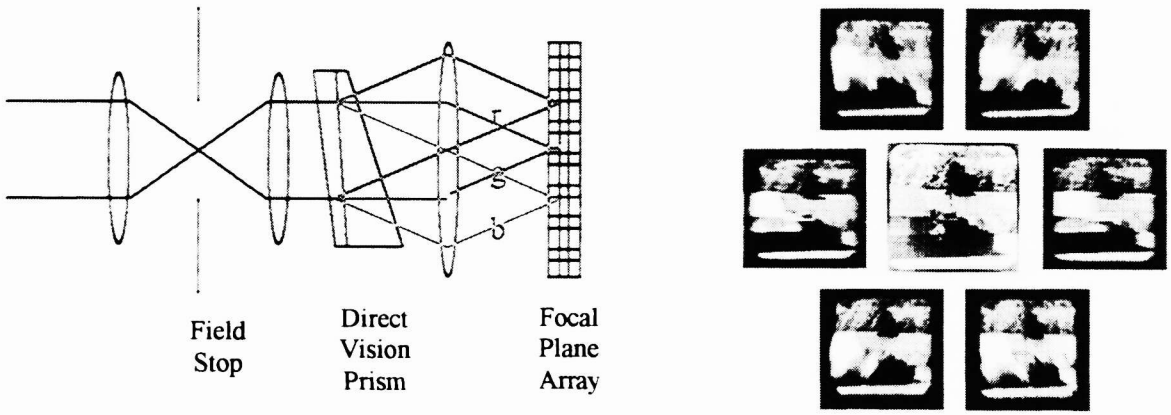

Figure 2: A schematic representation of the chromotomographic spectral imager. On the left, the direct view prism spreading red, green, and blue light across the FPA. On the right, six video frames demonstrating the effect of rotating prism dispersion on the measured image. In the center of these frames, is the reconstructed broad band image.

Figure 3(a) is a photograph of the SSSC VISNIR sensor head with a computer / controller / display system. Figure 3(b) is the sensor head with the telescope cover removed. The sensor head assembly consists of a variable frame camera and a telescope with an on-axis direct vision prism. A stepping motor that is synchronized with the camera drives the prism. The camera is based on a silicon 256 x 256 pn-junction focal plane array. The array output has an 8-bit dynamic range and a spectral range of 400-900 nm. The sensor has 64 spectral bands and variable frame rate up to 955 frames per second, corresponding to image cube rates up to 10 hypercubes per second. The sensor power supply provides a maximum of 20 watts of power, 5 watts for the motor to spin the prism and 15 watts for the camera. The camera/optics assembly is 4" high, 12" long, and 6" wide and weighs 4-6 pounds (depending on optics), with minimal attempt at miniaturization. These specifications do not include the sensor computer system. The supporting computer shown in Figure 3a is a Dell Precision 610 workstation

operating in a Unix environment. A laptop implementation of the supporting computer system is currently being developed for the VIS-NIR sensor.

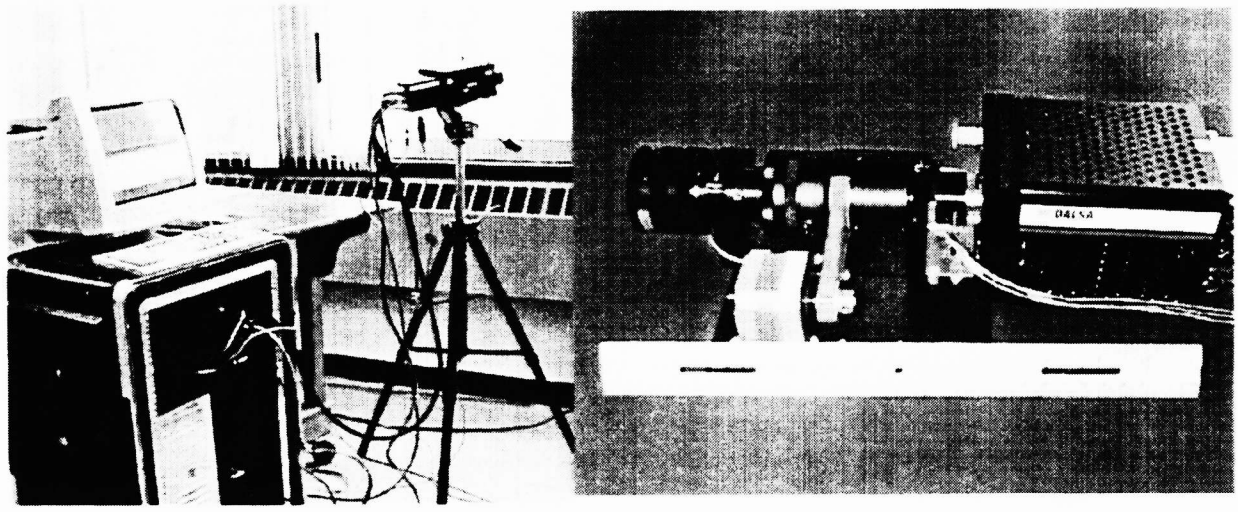

Figure 3: Photos of the Visible/NIR CTHIS instrument and supporting computer system on the left. A close-up of the sensor optics assembly and camera head is shown on the right.

3. DESCRIPTION OF THE RECONSTRUCTION ALGORITHM

This development follows Brodzik and Mooney.[4] A chromotomographic hyperspectral imaging spectrometer reconstructs a three dimensional spatial-chromatic scene from a sequence of two-dimensional images. The generic pseudo-inverse reconstruction algorithm is described in this section; however, the reconstruction can be accomplished using various approaches that depend on the constraints applied to the solution, and the level of fidelity required. Figure 2 describes the physical implementation of this computed-tomography image spectrometry approach. In this approach, a rotating prism accomplishes the multiplexing. As the prism rotates, each chromatic slice of the object cube follows a circular path with the radius of the path determined by the prism dispersion. A sequence of spatial tomographic projections $g(\bar{x}, \phi)$ is thus obtained, each tomographic projection being an integral of the three-dimensional spatial-chromatic object cube $f(\bar{x}, \lambda)$ in the chromatic variable λ.

$$g(\bar{x},\phi) = \int_{-\infty}^{+\infty} f(\bar{x} - k(\lambda - \lambda_0)\bar{p}_\phi, \lambda)d\lambda, \tag{1}$$

where $\bar{x} = (x_1, x_2)$, $\bar{p}_\phi = (\cos\phi, \sin\phi)$, $0 \le \phi < 2\pi$, λ_0 is the center wavelength, and k is a spectrometer constant determined by the sensor focal length and prism dispersion. The mathematics of sampling the object cube $f(\bar{x}, \lambda)$ to get the projection $g(\bar{x}, \lambda)$ is described schematically in Fig. 4. This operation can be recognized as a three-dimensional x-ray transform of $f(\bar{x}, \lambda)$, with integration performed over a line in direction $k\bar{p}_\phi$, where k determines the angle between the integration line and the optical axis. Taking the two-dimensional Fourier transform of Equation 1 in the spatial variable $\bar{x}$, we have,

$$g(\bar{\xi},\phi) = \int_{-\infty}^{+\infty} e^{-2\pi i \langle k\bar{p}_\phi, \bar{\xi}\rangle(\lambda-\lambda_0)} \mathbf{f}(\bar{\xi}, \lambda - \lambda_0)d\lambda, \tag{2}$$

where $\mathbf{f}(\bar{\xi}, \lambda)$ is the two-dimensional Fourier transform of $f(\bar{x}, \lambda)$ in $\bar{x}$, and $\bar{\xi} = (\xi_1, \xi_2)$ is the frequency variable. Consider a version of Equation 2, sampled at discrete chromatic bands and discrete angles,

$$g_m(\bar{\xi},\phi) = \sum_{n=0}^{N-1} e^{-2\pi i \langle \bar{p}_m, \bar{\xi} \rangle (n-n_0)} f_\eta(\bar{\xi}), \tag{3}$$

where $\bar{p}_m = (\cos\frac{2\pi m}{M}, \sin\frac{2\pi m}{M})$, $0 \le m < M$, $M \ge N$, $n = k\lambda$, $n_0 = k\lambda_0$, so

we have

$$\begin{bmatrix} g_0(\bar{\xi}) \\ g_1(\xi) \\ . \\ . \\ . \\ g_{M-1}(\bar{\xi}) \end{bmatrix} = A(\bar{\xi}) \begin{bmatrix} f_0(\bar{\xi}) \\ f_1(\xi) \\ . \\ . \\ . \\ f_{N-1}(\bar{\xi}) \end{bmatrix} \tag{4}$$

where the $\mathbf{A}(\bar{\xi})$ is an M x N matrix with elements

$$\mathbf{A}_{m,n}(\bar{\xi}) = e^{-2\pi i \langle \bar{p}_m, \bar{\xi} \rangle (n-n_0).} \tag{5}$$

For brevity we write Equation 5 as

$$g = Af. \tag{6}$$

The existence and uniqueness of the solution of Equation 6 depends on the rank of $\mathbf{A}$, which is equal to the number of independent rows of $\mathbf{A}$. Equation 5 shows that $\mathbf{A}$ is ill-conditioned for many values of $\bar{\xi}$. A convenient tool for evaluating the rank of a matrix is singular value decomposition (SVD). The singular value decomposition of a matrix $\mathbf{A}$ is defined[5] as

$$\mathbf{A} = \mathbf{U}\Sigma\mathbf{V}^H, \tag{7}$$

where $\mathbf{U}$ and $\mathbf{V}$ are M x N and N x N matrices, such that,

$$\mathbf{U}^H\mathbf{U} = \mathbf{V}\mathbf{V}^H = \mathbf{V}^H\mathbf{V} = \mathbf{I}, \tag{8}$$

The superscript H indicates Hermitian adjoint, and Σ is an N x N diagonal matrix of singular values,

$$\Sigma = \mathrm{diag}(\sigma_0, \sigma_1, \ldots, \sigma_{N-1}), \tag{9}$$

such that $\sigma_0 \ge \sigma_1 \ge \ldots \ge \sigma_{N-1} \ge 0$. If $\mathbf{A}$ is non-singular, i.e. $\sigma_0 \ge \sigma_1 \ge \ldots \ge \sigma_{N-1} \ge 0$, then a matrix inverse of $\mathbf{A}$ can be computed as

$$\mathbf{A}^{-1} = \mathbf{V}\Sigma^{-1}\mathbf{U}^H, \tag{10}$$

where elements of Σ^{-1} are found by inverting elements of Σ, and Equation 6 has a unique solution given by

$$f = \mathbf{A}^{-1}g. \tag{11}$$

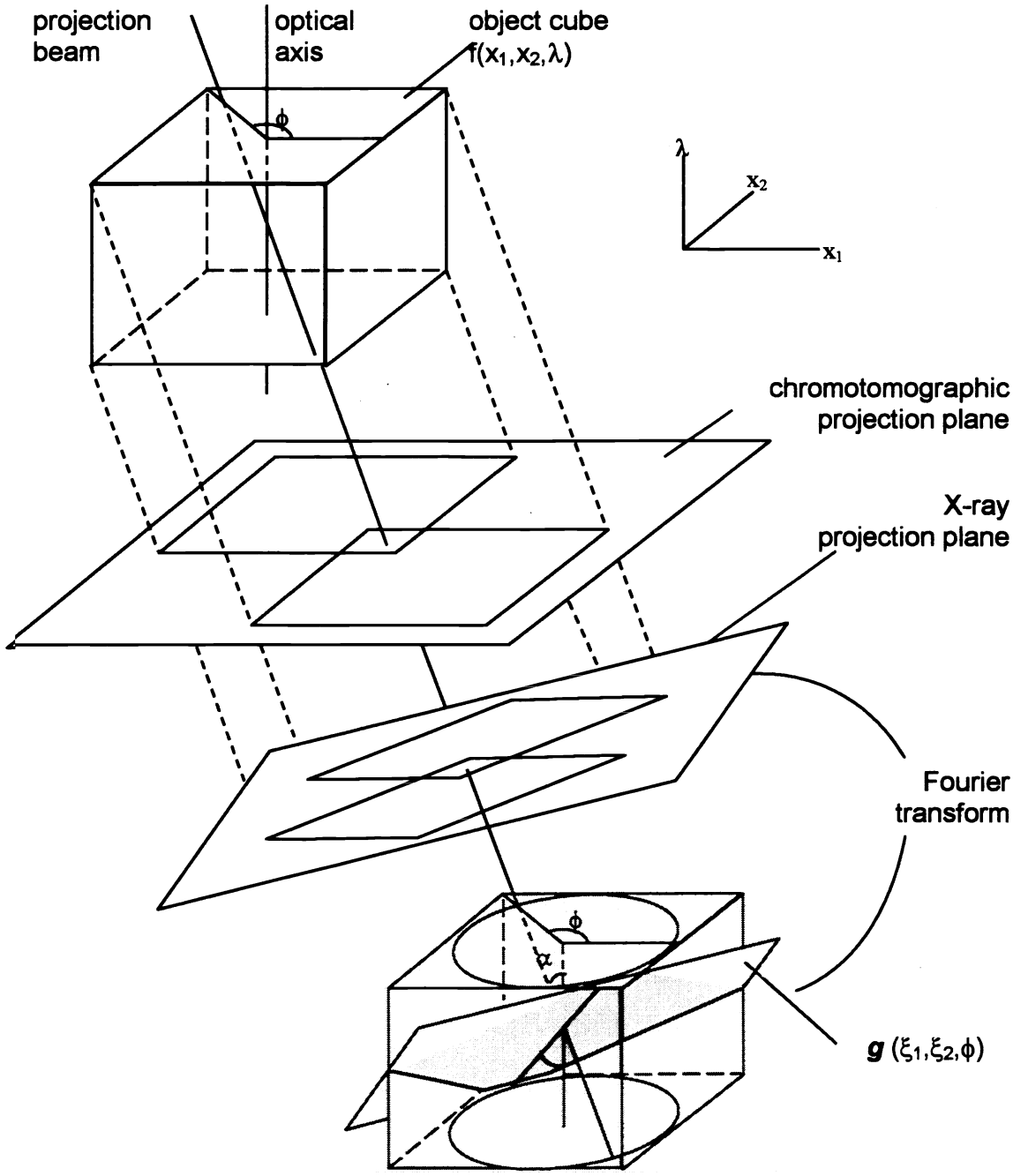

Figure 4: Geometry representing chromotomographic data collection and is relationship to the x-ray transform.

If **A** is singular, i.e. there is $K < N$ such that $\sigma_0 \geq \ldots \geq \_\sigma_{K-1} > \sigma_K = \ldots = \sigma_{N-1} = 0$,

$$\Sigma = \Sigma_k = \text{diag}(\sigma 0,\ldots,\sigma_{K-1}, 0,\ldots,0), \tag{12}$$

and a direct inverse $\mathbf{A}^{-1}$ cannot be obtained. Thus, Equation 6 cannot be solved uniquely. Alternatively, the Moore-Penrose inverse[6] (a pseudo-inverse) $\mathbf{A}^+$ can be used to find a minimum length least square solution of Equation 6. The pseudo-inverse of a matrix **A** is defined as

$$\mathbf{A}^+ = \mathbf{V}\Sigma^+ \mathbf{U}^H, \tag{13}$$

where the diagonal matrix Σ^+ is formed by replacing non-zero elements of Σ with the reciprocal values

$$\Sigma^+ = \text{diag}(\sigma_0^{-1},\ldots\sigma_{K-1}^{-1},0,\ldots,0). \tag{14}$$

Multiplying both sides of Equation 6 by $\mathbf{A}^+$ yields the pseudo-solution

$$\mathbf{f}^+ = \mathbf{A}^+\mathbf{g}. \tag{15}$$

In practice the recorded data **g** is contaminated by noise, n,

$$\mathbf{g} = \mathbf{Af} + \mathbf{n}. \tag{16}$$

In effect, small nonzero singular values of **A** result in instabilities. These instabilities can be considered by,

$$\mathbf{A}^+ \mathbf{g} = \mathbf{A}^+ \mathbf{Af} + \mathbf{A}^+\mathbf{n} = \mathbf{V}\Sigma^+ (\Sigma\mathbf{V}^H\mathbf{f} + \mathbf{U}^H\mathbf{n}). \tag{17}$$

If elements of Σ are close to zero, then elements of Σ^+ become very large and the filtered noise dominates the restoration. In order to balance the loss of spectral resolution and noise amplification due to small singular values, a modified version of Equation 10 can be used, where small singular values close to the noise variance are set to zero. Alternatively, a regularization technique can be applied, which allows for gradual transition of singular values to zero.[7] Nevertheless, the method of inversion, as implemented by Equation 11, leads to artifacts in the estimate of the hyperspectral image, particularly in scenes with a significant information content in the low spatial/high chromatic frequency regime, which coincides with the null space of **A**. To improve fidelity of the hyperspectral image, one needs to recover the null space information. This recovery of information can be done by using *a priori* information about the scene, such as finite extent, finite intensity range, energy bounds, etc., in the form of solution constraints. If the pseudo-solution does not meet these constraints, repetitive application of a sequence of constraints to the estimate leads to recovery of the null space information and to reduction of artifacts. These techniques are described in further detail in Brodzik and Mooney.[4]

4. POSITION AND WAVELENGTH DEGENERACY

There are two degenerate image classes that do not require a complete mathematical reconstruction, namely, the spectral analysis of a bright flash from a point source, and the position and wavelength determination of a monochromatic light source. In each of these cases, the information, in at least one dimension of the three-dimensional image cube, collapses to simplify the reconstruction. Therefore, analysis of radiation from point sources and monochromatic sources, such as lasers, can be performed in real time with substantially reduced computation.

In the case of the bright flash from a point source, the x- and y-dimensions give the source location, but there is no information about the spatial extension of the source. Therefore, the amount of spatial data to be processed can be reduced. It is assumed that the image of the scene is somewhat static and can be removed, by processes such as frame subtraction. Characterization of the event requires finding its location in two spatial dimensions and characterizing the temporal evolution of the spectral profile in two additional dimensions, wavelength and time.

Consider imaging a point source transient event with a chromotomographic sensor such as CTHIS. The intensity of the light from the point source is spread along the direction of the prism dispersion axis. The resulting line spectrum is a record of the source spectral signature, at that instant in time. For a framing sensor, we record the average spectral signature over a video frame interval. The evolution of the source signature with time is recorded by the collection of line spectra from successive video frames. These spectra can be corrected, for presentation along a single axis, by a simple angle transformation. The background scene clutter is removed by subtracting consecutive frames, for a given prism orientation. The evolution of clutter is minimal at high prism rotation rates. After the clutter is removed, the transient event appears as a line segment on the preprocessed imagery, as shown schematically, in Figure 5. As the prism rotates, the axis of dispersed light rotates. The intersection of the dispersed line segments from different frames identifies the location of the transient event, and the center wavelength of the direct vision prism. Thus, a four-dimensional x-y-λ-t measurement of the transient event is accomplished.

Although the data processing load is greatly reduced, hyperspectral point event characterization is a four-dimensional problem. Scanned slit, interferometric, and variable filter techniques are ill suited for this task since their multiplexing techniques fail to uniquely encode the spatial-temporal-spectral signature of the event.

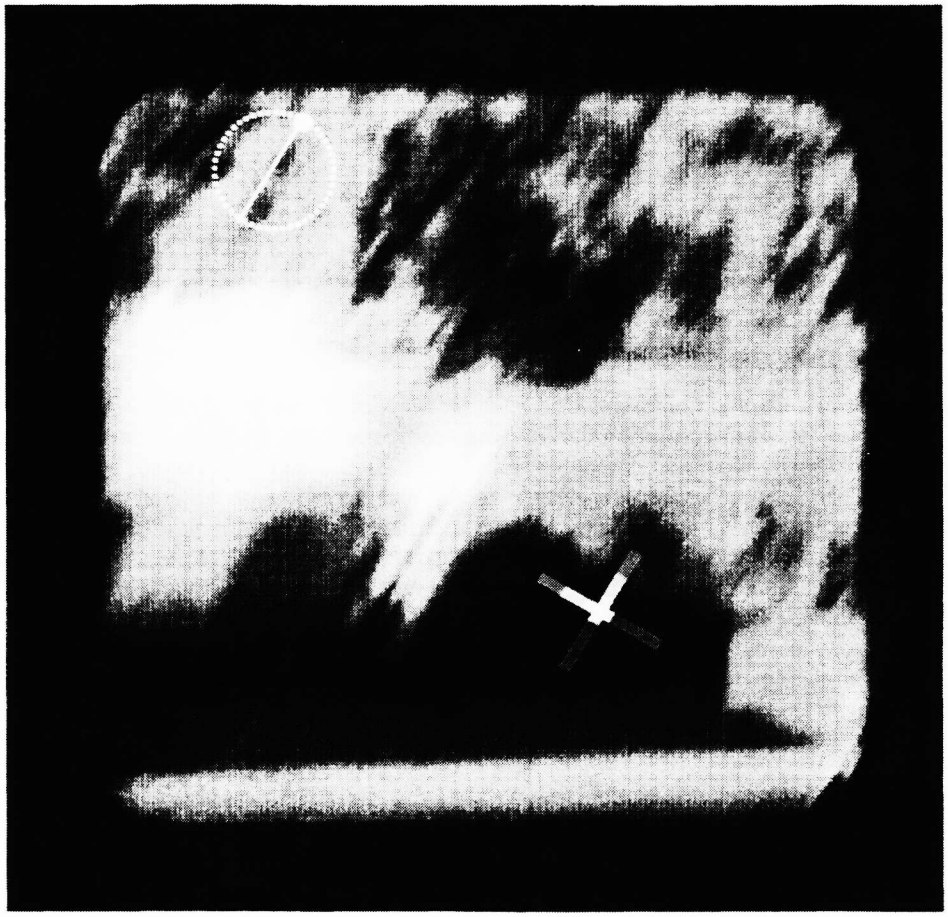

Figure 5: Unreconstructed image as seen through the direct view prism. The spectrum of a high intensity point source is schematically illustrated as a rainbow line superimposed on the original image. The second rainbow line illustrates the line spectrum in a later frame, of different prism orientation. The intersection of the two rainbow lines defines the location of the point source. The spectrum and location of a monochromatic light source is shown as a locus of points, from successive video frames that form a circle. The origin of the circle is determined by the location of the light source and the radius of the circle is determined by the wavelength of the radiation.

In the case of a highly monochromatic light source, such as a laser, the λ-dimension collapses leaving only the spatial information of the scene. Hyperspectral monochromatic light characterization is also a four-dimensional problem that requires finding the location of the event in two spatial dimensions, as well as measuring a short-pulsed spectral line (two additional dimensions). Scanned slit, interferometric, and variable filter techniques are unlikely to capture short-pulsed monochromatic illumination across a spectral band.

The direct view prism blurs all broadband light sources, however, monochromatic light sources such as LEDs and LASERs are shifted in the direction of the prism orientation, rather than blurred. As the prism is rotated, the monochromatic light source traces out a series points that form a circle on the imaging array (cf. Fig. 5). The circle is a record of the spectral signature of the monochromatic light source over an interval in time. The origin of the circle is identifies the location of the light source and the radius of the circle is identifies the wavelength of the radiation.

5. LIGHT EMITTING DIODE MEASUREMENTS

An LED test source was fabricated to evaluate the sensor imaging performance and spectral resolution. The configuration of this source and particular LED wavelengths are shown in Figure 6. A reconstructed image of the test source is given in Figure 7. We note that the optics were not color corrected, consequently, images of some of the LEDs are out of focus. Figure 8 is a 2-dimensional scatter plot of the data, which was obtained by rotating an n-dimensional representation of the image until good separation was obtained between clusters. The axis of the plot correspond to Eigen-spectra of the image. Each point in the plot corresponds to a particular pixel in the image and the point coordinates represent the fraction of each Eigen-spectra at that pixel. The dense central cluster is associated with the image background, or box, signature. The spoke patterns are associated with LEDs of a particular wavelength. The LED signatures are not tightly clustered, corresponding to the moderately broad spectra of the LEDs.

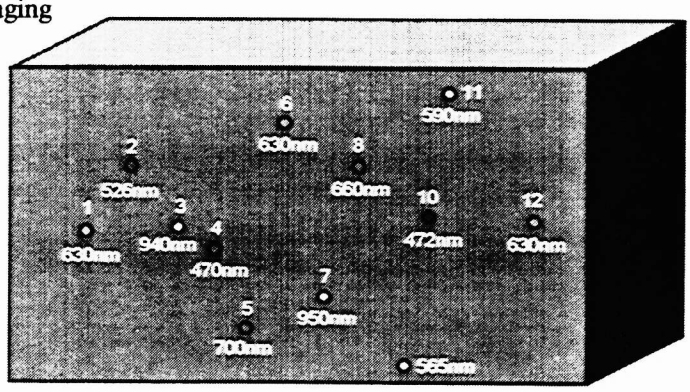

Figure 6: Diagram of LED box used as a source of spectral data.

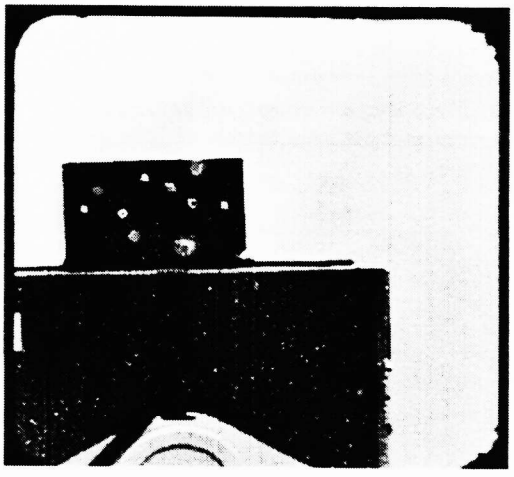

Figure 7: Broadband reconstruction of the image of the LED test source.

Figure 8: A 2-dimensional scatter plot from the hyperspectral image cube of the LED test source.

Figure 9 gives the measured spectra for the set of diodes in the test source. We note that good resolution is obtained for diodes having peak separations ranging from 25 nm to 50 nm. The horizontal scale is linear in band number but not linear in wavelength; consequently, the LEDs at 472 nm appear broader than the LEDs at 700 nm. In fact, the measured LED spectrum as measured by CTHIS shows the shorter wavelength devices are narrower than the longer wavelength devices. In Figure 10, we give the manufacturers spectral output data for the 472 nm and 526 NM diodes. After accounting for the nonlinear horizontal axis in Figure 9, it can bee seen that there is good agreement between the hyperspectral sensor measurements and the manufacturers specification.

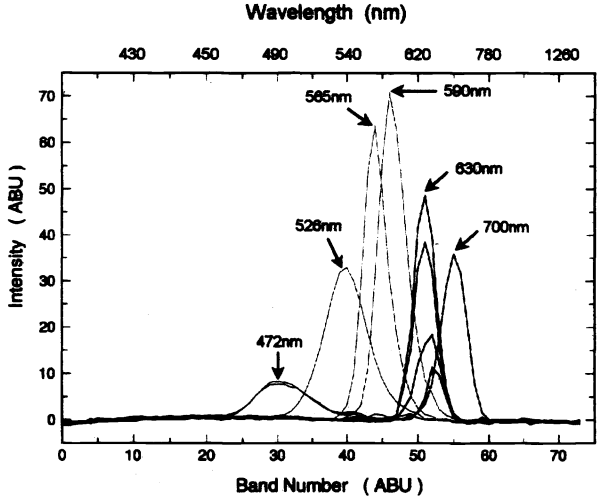

Figure 9: Measured spectral output from the LEDs of the test source array.

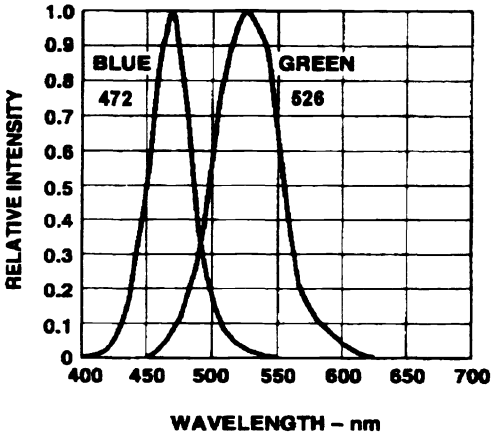

Figure 10: Manufacturers published spectra for 472 nm and 526 nm LEDs of test source.

6. HYPERSPECTRAL IMAGE CUBE MEASUREMENTS

Figure 11a shows a hyperspectral image cube data, from a sunlit scene in Lincoln Massachusetts. The full data cube image includes 64 spectral slice images of the scene. These slices can be displayed as single narrow band images. As an example, in Fig. 11b we show the narrow band image slice from sensor band number 58, which is near 750 nm wavelength. The set of narrow band images can be used to reconstruct a broadband image, giving a result similar to a normal video camera image. Alternatively, a special sub-set of spectral slices could be assembled, to optimize the signal to noise, or contrast, of a particular type of obect or substance, within the scene.

We have measured the spectrum of four points in the scene of Fig. 11, a sunlit tree, grass, an asphalt road and a metal cylinder. The location of these measurement are indicated in Figure 11(b). The spectrum of each of these objects is given in Figure 12 In Fig. 12, the camera spectral band number is given at the bottom and the wavelength scale is given at the top. We note that there is substantial reduction in spectral resolution at long wavelengths. A new direct vision prism set has been designed to improve long wavelength resolution.

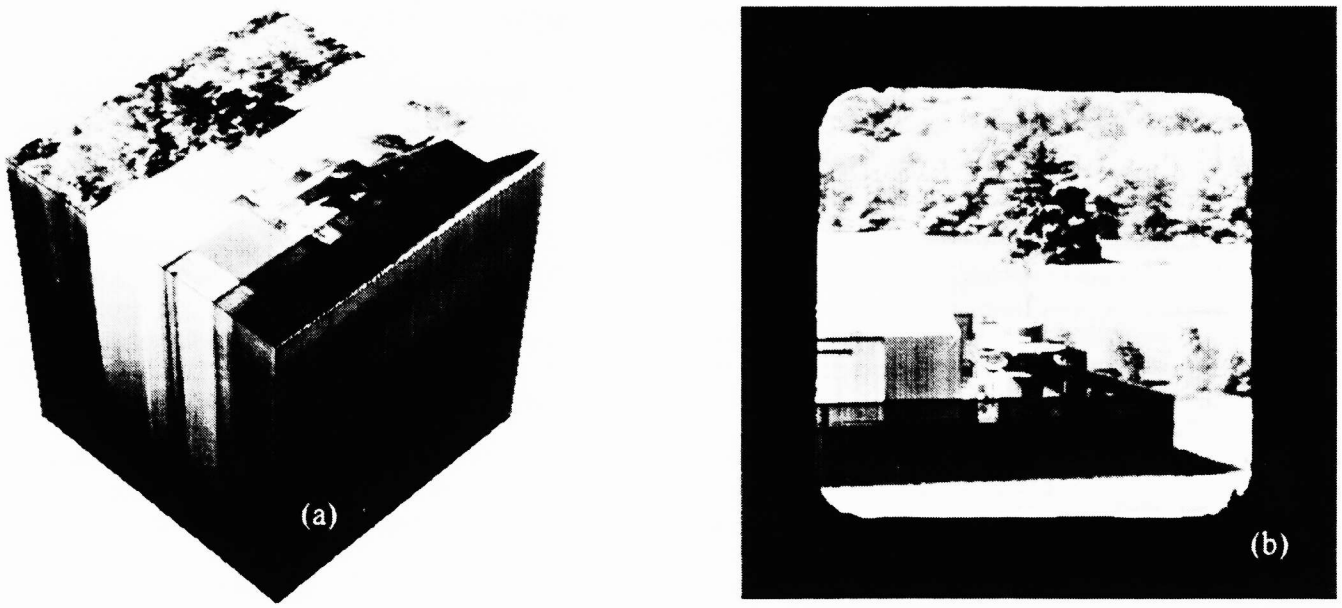

Figure 11: (a) An image data cube from a sunlit scene. (b) Spectral band image (number 58), near 750 nm, taken from Visible-NIR CTHIS image data cube. There are four pixel locations are identified by crosses.

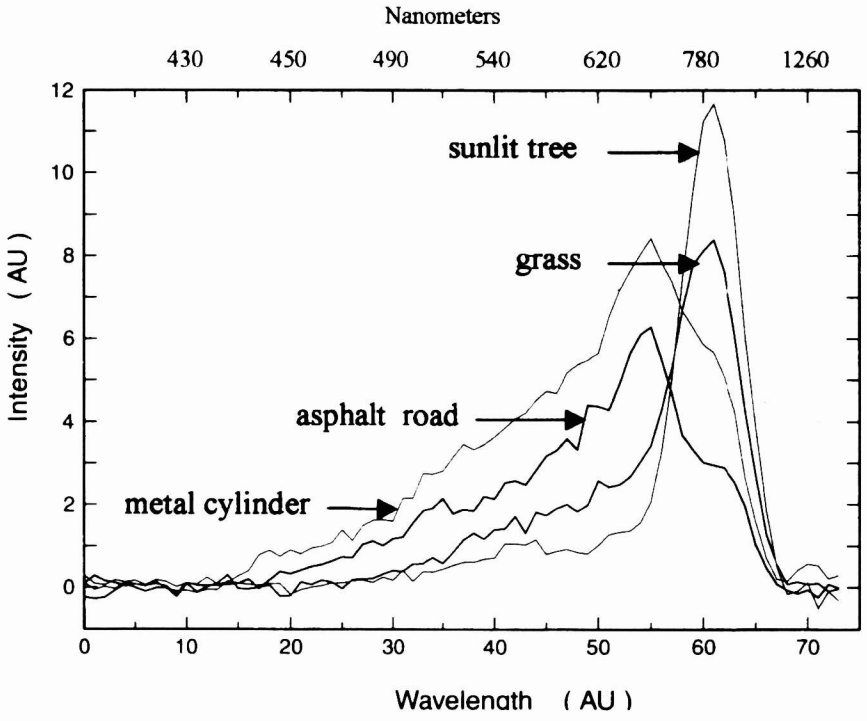

Figure 12: The measured spectra at the locations indicated in Fig. 11b.

7. CONCLUSIONS

We have developed a visible to near infrared staring-mode hyperspectral imaging sensor based upon the architecture of the chromotomographic hyperspectral imaging sensor of Mooney, et al. The Visible/NIR band was selected by SSSC because the many applications of hyperspectral imaging in this band and because of the availability of low cost optical materials and small, high-speed, low cost cameras.

The Vis-NIR hyperspectral imager consumes less than 20 W of power, less than 5 W for the motor to spin the prism and less than 15 W for the camera. The laboratory sensor is 4" high, 12" long, 6" wide and weighs less than 6 pounds, with minimal attempt at miniaturization. Sensor specifications include a 256x256, 8-bit imaging array, 64 spectral bands in a spectral range of 400-900 nm and frame rates up to 955 Hz, corresponding to image cube rates up to 10 hypercubes/sec. We note that general hyperspectral scenes would be characterized at the hypercube rate, but degenerate signals, such as those from point sources or monochromatic sources, could be characterized at rates approaching the camera video frame rate of 955 Hz.

We have provided initial sensor data including the spectra and a scatter plot diagram, derived from the principal component analysis, of an array of dissimilar light emitting diodes. We have also presented "as measured" rotating axis dispersed imagery of a scene and the associated reconstructed broadband image of the scene, which has minimal artifacts.

We believe the VIS-NIR CTHIS sensor will provide a baseline for compact, light weight, hyperspectral imaging systems suitable for a wide range of applications on ground, sea, air or space platforms.

The authors would like to thank Steven DiSalvo for the construction of the LED source, Virgil Vickers for his recommendations and Linda Bouthillette for graphics support.

REFERENCES

[1] J. M. Mooney, V .E. Vickers et al., "High Throughput Hyperspectral Infrared Camera", J. Opt. Soc. Am., A, Vol. 14, No. 11, pp. 2951-2961, November 1997.

[2] J. M. Mooney and T. D. Reeves, Private communication, 1999.

[3] J. M. Mooney, "Angularly multiplexed spectral imager," Imaging Spectrometry, Ed. M. R. Descour, J. M. Mooney, D. L. Perry and L. Illing, Proc. SPIE, Vol. 2480, pp. 65-77, 1995.

[4] A. K. Brodzik and J. M. Mooney, "Convex projections algorithm for restoration of limited angle chromotomographic images", J. Opt. Soc. Am. A, Vol. 16, No. 2, pp. 246-257, February 1999.

[5] G. Golub and C. Van Loan, Matrix Computations, Johns Hopkins University Press, Baltimore, MD 1993.

[6] A. Ben Israel and T. N. E. Greville, Generalized Inverses: Theory and Applications, Wiley, New York, NY, 1980.

[7] A. Sano, "Optimally regularized inverse of singular value decomposition and application to signal extrapolation," Signal Processing, Vol. 30, pp. 163-176, 1993.